https://doi.org/10.5194/egusphere-2025-3254
Preprint. Discussion started: 13 August 2025

Impacts of Thermodynamic and Dynamic Processes on the Vertical Distribution of Carbonaceous Aerosols: lessons from in-situ observations at eastern foothills of LiuPan Mountains, Loess Plateau

Shaofeng Qi[1, 2], Suping Zhao [1, 3*], Ye Yu[1, 3], Longxiang Dong[1, 3], Tong Zhang[1, 3], Guo Zhao[1, 2, 3], Jianglin Li[1, 3], Xiang Zhang[1, 2], Yiting Lv[1, 2]

1. Key Laboratory of Cryospheric Science and Frozen Soil Engineering, Northwest Institute of Eco-Environment and Resources, Chinese Academy of Sciences, Lanzhou 730000, China.

2. University of Chinese Academy of Sciences, Beijing 100049, China.

3. Pingliang Land Surface Process & Severe Weather Research Station, Pingliang 744015, China.

Correspondence to: Suping Zhao (zhaosp@lzb.ac.cn)

Abstract. The vertical distribution of carbonaceous aerosols critically influences planetary boundary layer structure and climate impacts. However, high-resolution vertical data remain scarce over the Chinese Loess Plateau. To address this gap, coordinated observations of carbonaceous aerosols and meteorological variables were conducted in the Loess Plateau using tethered balloon-borne instruments during two field campaigns in July 2023 and 2024. The average near-surface concentrations of black carbon (BC) and ultraviolet particulate matter (UVPM) in Pingliang were 0.82 μg m^{-3} and 1.26 μg m^{-3}, respectively. Vertically, carbonaceous aerosol concentrations generally decreased with height. A comparison of the vertical profiles of BC, UVPM, VTKE (mechanical turbulence), and potential temperature showed that during the early morning and nighttime, when convective activity was weak, UVPM concentrations in the upper atmosphere were higher than those of BC. This pattern is primarily attributed to nucleation processes involving gaseous precursors during nighttime. Analysis of the roles of dynamic and thermodynamic processes indicated

https://doi.org/10.5194/egusphere-2025-3254
Preprint. Discussion started: 13 August 2025

that thermodynamic processes dominated aerosol vertical transport in the near-surface layer, while enhanced dynamic processes at higher altitudes facilitated horizontal dispersion of pollutants. Air masses from the south of the observation site contributed significantly to UVPM levels. As air mass altitude decreased, the influence of local sources became more pronounced. Overall, this study demonstrated the regulatory mechanism of daytime and nighttime thermodynamic and dynamic impacts on the vertical distribution of pollutants.

1. Introduction

Carbonaceous aerosols, particulate matter generated from fossil fuel combustion and biomass burning, directly impact the Earth-atmosphere energy budget by absorbing solar radiation. Their primary components are organic carbon (OC) and black carbon (BC). OC encompasses both primary organic carbon (POC) emitted directly from biomass burning and secondary organic carbon (SOC) formed through the photochemical reactions of volatile organic compounds (VOCs). Due to its complex chemical composition, OC introduces substantial uncertainty in climate effect assessments (Kroll et al., 2011). Black carbon (BC), characterized by strong solar radiation absorption, represents the second-largest anthropogenic climate forcer after CO_2 (Bond et al., 2013; Ramanathan & Carmichael, 2008). Near the base of the stratosphere, BC's direct radiative forcing can be approximately ten times stronger than at the surface (Samset & Myhre, 2011). Consequently, its vertical position within the atmosphere significantly influences atmospheric stratification (Zhang et al., 2017; Zhao et al., 2021). Within the surface layer, BC can heat the lower atmosphere, enhancing convection and promoting boundary layer development. At higher altitudes, however, BC heats the atmosphere while simultaneously reducing solar radiation reaching the surface, leading to increased atmospheric stability. This suppresses boundary layer development and exacerbates air pollution (Ding et al., 2016; Petäjä et al., 2016; Wang et al., 2018a). Over complex terrain, valley wind systems and orographically-induced turbulence can transport surface-emitted BC to

https://doi.org/10.5194/egusphere-2025-3254
Preprint. Discussion started: 13 August 2025

higher elevations, where it accumulates within temperature inversion layers. Absorptive BC further heats the atmosphere, suppressing the development of the planetary boundary layer (PBL) and altering its height and stability (Zhao et al., 2023). Additionally, BC modifies cloud microphysical properties, influencing cloud formation, dissipation, and precipitation, thereby affecting regional and global climate systems (Panicker et al., 2014; Wendisch et al., 2008). Over recent decades, the radiative forcing and climate effects of BC have been extensively studied. Published estimates of BC's direct radiative forcing range between 0.25–0.90 W m^{-2} (Allen & Landuyt, 2014), yet these values are subject to considerable uncertainty. A primary source of this uncertainty is the significant spatiotemporal heterogeneity of BC at the global scale, stemming from regional combustion processes and its short atmospheric lifetime. Consequently, using default model BC profiles to simulate radiative forcing introduces substantial errors (Hodnebrog et al., 2014). Reported studies indicate that differences in BC vertical distribution contribute approximately 20–40% to the uncertainty in calculations of BC's top-of-atmosphere radiative forcing (Chen et al., 2022; Zarzycki & Bond, 2010). Therefore, accurately characterizing the true vertical distribution of BC in the atmosphere is crucial for the precise assessment of its regional and global climate effects.

However, acquiring accurate BC vertical profiles remains a significant challenge for researchers globally. Current observation methods include: Tethered balloons (Guan et al., 2022; Wang et al., 2021a; Zhao et al., 2023), Aircraft measurements (Moorthy et al., 2004; Schwarz et al., 2017), Unmanned Aerial Vehicles (UAVs) (Liu et al., 2020; Wang et al., 2021b; Wu et al., 2021), Cable cars (Zawadzka et al., 2017), Meteorological towers (Wang et al., 2018b; Xie et al., 2019), Topography-dependent in-situ observations (Zhao et al., 2019; 2022). Notably, aircraft measurements face operational constraints in complex terrain due to high costs and requirements for expansive landing areas. UAVs, cable cars, and meteorological towers are limited by maximum achievable altitudes – most UAVs typically reach only ~500 m, while cable cars and towers cover even lower vertical ranges. Though topography-dependent

https://doi.org/10.5194/egusphere-2025-3254
Preprint. Discussion started: 13 August 2025

observations are widely applied in complex terrain, their coarse spatial resolution cannot resolve true vertical distributions of atmospheric constituents. Additionally, while lidar remote sensing enables continuous profiling (Miffre et al., 2015), its accuracy remains inferior to in-situ techniques. In contrast, tethered-balloon systems mitigate these key constraints by providing high-resolution BC profiles within the planetary boundary layer. This approach has been successfully deployed across diverse regions including Europe, the Arctic, South Asia, and China's North China Plain, Sichuan Basin, and Yangtze River Delta (Bisht et al., 2016; Mazzola et al., 2016; Ran et al., 2016; Samad et al., 2020; Wang et al., 2018b).

Pingliang City, situated in eastern Gansu Province, lies at the convergence of Shaanxi, Gansu, and Ningxia provinces. As a significant component of the Loess Plateau and a major agricultural zone in Northwest China, understanding its climatic-environmental mechanisms is crucial for improving meteorological forecasting accuracy and formulating effective pollution control strategies. The region's complex topography facilitates the transport of urban pollutants to higher-elevation loess tablelands via valley wind circulations, enabling dispersion during transit. Furthermore, influenced by the towering Liupan Mountains, Pingliang exhibits pronounced vertical climatic heterogeneity, resulting in intricate feedback mechanisms between the planetary boundary layer and aerosols. Current research reveals scarce data on the vertical distribution of BC from fossil fuel combustion, biomass burning, and mineral dust activities in this region. To address this gap, we conducted detailed vertical profile observations using tethered balloon-borne instrumentation over typical loess tableland areas during July 2023 and July 2024. This study aims to supplement the deficiency in local BC aerosol observations, establish a database for assessing aerosol climate effects on the Loess Plateau, and ultimately provide scientific foundations for pollution control strategies.

2. Materials and methods

https://doi.org/10.5194/egusphere-2025-3254
Preprint. Discussion started: 13 August 2025

2.1 Observation methods and data sources

Field observations were conducted at the Pingliang Land Surface Processes and Severe Weather Research Station (Pingliang Station), Chinese Academy of Sciences, during two intensive campaigns from 15 to 24 July 2023 and 17 to 30 July 2024. The station is located in Baimiao Township, Pingliang City, Gansu, with geographic coordinates detailed in Figure 1. Near-surface meteorological parameters at Pingliang Station and the Air Quality Index (AQI) for Pingliang City during the observation periods are presented in Figure S1, while Figure S2 displays concentrations of PM_{10}, $PM_{2.5}$, CO, SO_2, NO_2, and O_3 in Pingliang's urban area. Meteorological data were obtained from near-surface observations at Pingliang Station, and air quality measurements originated from the Pingliang Environmental Monitoring Station (Station ID: 2656A; http://eia-data.com/). Results indicate that southeasterly or northwesterly winds prevailed at Pingliang Station during the observation periods, with wind speeds typically below 1 m s^{-1}. The mean temperature was 20.76°C and mean relative humidity was 76.84%. Air quality in Pingliang remained generally good except during sporadic dust pollution events.

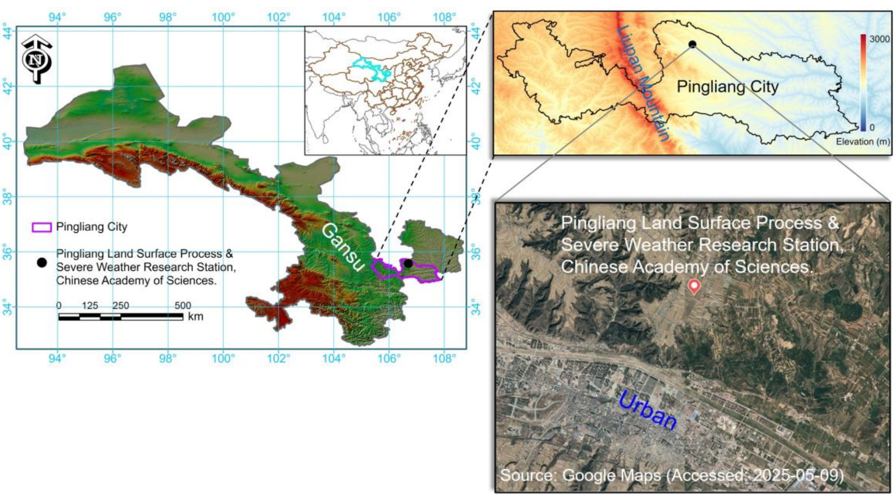

Figure 1. Geographic location of the observation site. The map is a pure reproduction of Google Maps with added marks for our study locations. Copyright © Google Maps. Publisher's note: Please note that the above figure contains disputed territories.

https://doi.org/10.5194/egusphere-2025-3254
Preprint. Discussion started: 13 August 2025

2.1.1 Tethered balloon platform

Vertical profiling was primarily conducted using instrumentation suspended from a tethered balloon system. The system comprised a 10 m³ helium-filled balloon, a tether line, and an electrically powered winch that actively regulated both ascent and descent rates. Buoyancy provided initial lift, while the winch precisely controlled vertical maneuvering. Instruments were mounted 30 m below the balloon to minimize direct atmospheric disturbance. A MicroAeth® MA350 aerosol monitor measured vertical distributions of carbonaceous aerosols, and an iMet-4 radiosonde (iMet, USA) acquired temperature and humidity profiles. Observations were conducted at 3-hour intervals from 05:00 to 23:00 local time (05:00, 08:00, 11:00, 14:00, 17:00, 20:00, 23:00) daily. Operations were suspended during adverse conditions (e.g., strong winds or precipitation). Complementary vertical wind profiles were obtained using Doppler Beam Steering (DBS) mode of a Leosphere Windcube 200s lidar. Each balloon sounding lasted approximately 30–60 minutes, during which atmospheric conditions remained relatively stable, allowing both ascent and descent paths to characterize vertical structures. A total of 24 and 39 soundings were completed during summer 2023 and 2024 respectively, yielding 126 vertical atmospheric profiles.

2.1.2 Carbonaceous aerosol mass concentrations

The MicroAeth® MA350 determines BC concentration based on the Beer-Lambert law, quantifying light absorption by carbonaceous particles deposited on a PTFE filter at multiple wavelengths. The instrument employs five laser wavelengths: 375 nm (UV), 470 nm (Blue), 528 nm (Green), 625 nm (Red), and 880 nm (IR). Carbon concentration measured at 880 nm is considered equivalent to BC concentration (denoted as IRBC or BC) (Zhao et al., 2023), while measurements at 375 nm represent Ultraviolet Particulate Matter (UVPM) associated with biomass combustion (e.g., wood, straw). The Ångström Absorption Exponent (AAE), calculated from multi-wavelength measurements, characterizes the wavelength dependence of carbonaceous aerosol absorption. During this study, the MA350 operated at a flow rate of 150 mL min^{-1} with a 5-second sampling interval. Negative optical attenuation

https://doi.org/10.5194/egusphere-2025-3254
Preprint. Discussion started: 13 August 2025

(ATN) values occasionally occurred under low aerosol concentrations at high altitudes, which were corrected using the Optimized Noise-reduction Averaging (ONA) algorithm (Hagler et al., 2011).

2.2 Calculation of light absorption coefficient for carbonaceous aerosols

The light absorption coefficient (b_{Abs}) of black carbon was calculated using the following Eq. (1):

$$b_{Abs} = MAC_{BC}(\lambda)\times[BC] \quad (1)$$

where $MAC_{BC}(\lambda)$ denotes the mass absorption cross-section of BC at specific wavelengths. For the MicroAeth® series instruments, the MAC values at 375 nm, 470 nm, 528 nm, 625 nm, and 880 nm are 24.07 $m^2\ g^{-1}$, 19.07 $m^2\ g^{-1}$, 17.03 $m^2\ g^{-1}$, 14.09 $m^2\ g^{-1}$, and 10.12 $m^2\ g^{-1}$, respectively (Zhao et al., 2023). The [BC] represents the mass concentration of BC.

Additionally, the light absorption coefficient of BC can be expressed as:

$$b_{Abs}(\lambda) = k \times \lambda^{-AAE} \quad (2).$$

In Eq. (2), k is a wavelength-independent constant, and AAE represents the Ångström Absorption Exponent, which characterizes the wavelength dependence of BC's light absorption. A higher AAE value signifies that the aerosol absorption capacity decreases more rapidly with increasing wavelength. By combining the b_{Abs} values derived from Eq. (1) with Eq. (2), vertical profiles of AAE for BC were obtained.

2.3 Determination of planetary boundary layer height

Potential temperature (θ, in K), defined as the temperature an air parcel would attain if adiabatically brought to a standard pressure level (Han et al., 2019; Seidel et al., 2010), is calculated as Eq. (3):

$$\theta = (T+273.15) \times \left(\frac{P_0}{P}\right)^{\frac{R_d}{C_{pd}}} \quad (3)$$

where T denotes measured air temperature (°C), P represents air pressure (hPa), P_0 is the standard reference pressure (1000 hPa), R_d signifies the gas constant for dry air

https://doi.org/10.5194/egusphere-2025-3254
Preprint. Discussion started: 13 August 2025

($287\ J\ kg^{-1}\ K^{-1}$), and C_{pd} corresponds to the specific heat of dry air at constant pressure ($1005\ J\ kg^{-1}\ K^{-1}$).

Specific humidity (q, $g\ g^{-1}$), defined as the ratio of water vapor mass to the total mass of moist air (water vapor plus dry air), is calculated using Eq. (4),

$$q = \frac{\varepsilon \times e}{P - 0.378 \times e} \quad (4)$$

where ε = 0.622, e represents vapor pressure, and P denotes atmospheric pressure, with vapor pressure, e being derived from Eq. (5) through relative humidity (RH) and air temperature (T, °C).

$$e = 6.105 \times RH \times \exp\left(\frac{17.7 \times T}{237.7 + T}\right) \quad (5).$$

The planetary boundary layer (PBL) refers to the lower troposphere directly influenced by surface forcing with a response time of less than one hour, playing a critical role in the dispersion and transport of air pollutants. Within the PBL, turbulent mixing processes homogenize air temperature and humidity, resulting in relatively uniform distributions of these properties. Distinct discontinuities in temperature, humidity, and wind speed typically mark the PBL top (Emeis et al., 2008; Seibert et al., 2000). While various methodologies exist for determining PBL height (PBLH), this study employs two established approaches: the potential temperature gradient method and the parcel method, with detailed computational procedures provided in Supplementary Table S1 (Zhang et al., 2020)

2.4 Impacts of thermodynamic and dynamic processes on vertical distribution of carbonaceous aerosols

To quantify the relative contributions of potential temperature gradient, mechanical turbulence index, horizontal wind speed, and vertical wind speed to UVPM variations at different altitudes, we employed a random forest regression algorithm. The model generated training subsets via bootstrap sampling, with random feature subsets selected for optimal splitting at each decision tree node. Observations were

https://doi.org/10.5194/egusphere-2025-3254
Preprint. Discussion started: 13 August 2025

categorized into daytime (08:00, 11:00, 14:00, 17:00 LT) and nighttime (20:00, 23:00, 05:00 LT) periods to compare the dominant mechanisms governing aerosol vertical distribution. The mechanical turbulence index was calculated using Eq. (6).

$$V_{TKE} = 0.5 \times \sqrt{\overline{u}^2 + \overline{v}^2 + \overline{w}^2} \quad (6).$$

2.5 Identification of potential source regions

In this study, GDAS1 meteorological data (1° × 1° resolution) obtained from the NOAA FTP repository (ftp://arlftp.arlhq.noaa.gov/pub/archives/gdas1) were utilized. These data were processed using the MeteoInfo software to calculate backward trajectories and perform cluster analysis (http://www.meteothink.org/). Subsequently, the potential source contribution function (PSCF) and concentration weighted trajectory (CWT) analysis toolkits within MeteoInfo were employed to identify potential source regions and quantify their relative contributions (Wang, 2014).

3. Results and discussions

3.1 Vertical profiles of carbonaceous aerosols

3.1.1 General characteristics of BC

Observations indicate that near-surface mass concentrations of BC and UVPM averaged 0.82 μg m^{-3} and 1.26 μg m^{-3}, respectively. During the campaign, UVPM concentrations varied between 0.21 and 5.63 μg m^{-3} across different altitudes, whereas BC ranged from 0.13 to 2.05 μg m^{-3}. Compared with previous studies conducted in other regions of China, the concentration of BC observed in Pingliang is lower than those reported in Beijing, Shanghai, Nanjing, Chengdu, Shenzhen, Hengshui, the Beibu Gulf region, and Lanzhou (Guan et al., 2022; Ran et al., 2016; Shi et al., 2021; Wang et al., 2021a; Wu et al., 2021; Yang et al., 2023; Yang et al., 2022; Zhao et al., 2023). This discrepancy can be attributed to several factors. Firstly, Pingliang is a relatively small city with a permanent population of fewer than 2 million, whereas the aforementioned cities have much larger urban populations. Consequently, the total amount of air pollutants generated from daily human activities

https://doi.org/10.5194/egusphere-2025-3254
Preprint. Discussion started: 13 August 2025

in Pingliang is comparatively lower. Secondly, the observation site in Pingliang is situated at a higher elevation than the urban center, thereby reducing the influence of direct urban emissions. In contrast, observation sites in other cities are typically located in suburban areas that are more directly affected by emissions from urban cores. Wang et al. (2019) conducted tethered-balloon measurements of the vertical distribution of BC over the Tibetan Plateau and found even lower BC concentrations than those in the present study. Furthermore, the rate of decrease in BC concentrations with altitude was more pronounced at the Plateau site compared to Pingliang. Overall, existing studies consistently indicate that BC concentrations decrease with increasing altitude. However, due to differences in terrain, PBLH, and atmospheric diffusion conditions, the vertical profiles of BC vary significantly among different sites. For instance, in Shanghai, Wang et al. (2021a) reported a sharp decline in BC concentrations at around 600 m in the morning, while in the afternoon, the decrease occurred at approximately 800 m due to stronger convective mixing. Over the Tibetan Plateau, BC concentrations dropped markedly at altitudes as low as 100–200 m (Wang et al., 2019). Yang et al. (2023) and Zhao et al. (2023) reported elevated BC concentrations near 2000–2500 m, which they attributed to the combined effects of upper-level subsidence and lower-level updrafts. Similarly, Lu et al. (2019) and Chen et al. (2022) observed elevated BC concentrations in the 500–800 m layer over Anhui and Beijing, respectively, primarily influenced by the presence of upper-level temperature inversions.

From the global perspectives, the near-surface BC concentration in Delhi, India, was reported to be approximately 30.00 μg m^{-3}, which is substantially higher than those observed in China and Europe (Bisht et al., 2016). In contrast, near-surface BC concentrations in Stuttgart, Germany, and Milan, Italy, were found to be comparable to those in Shenzhen, China, at around 2.00–3.00 μg m^{-3}. These values are lower than those reported in other Chinese cities such as Shanghai, Nanjing, Chengdu, Hengshui, and Lanzhou, but still higher than the concentrations observed in this study (Ferrero et al., 2011; Samad et al., 2020). In the Arctic region, due to limited anthropogenic

https://doi.org/10.5194/egusphere-2025-3254
Preprint. Discussion started: 13 August 2025

influence, near-surface BC concentrations are generally lower than those observed both over the Tibetan Plateau in China and in the Loess Plateau region investigated in this study (Ferrero et al., 2016).

3.1.2 Diurnal variations of BC and UVPM profiles

Figures S3 and S4 respectively depict the trends and correlations of the ascent and descent profiles for BC and UVPM. The results indicate that ascent and descent profiles in this study exhibit very similar trends with only minor differences, warranting their combination into a single mean profile. Figure 2 shows the averaged profiles for all sampling periods during the observation campaign, including both ascent and descent legs of the tethered balloon. In Figure 2, the red solid line and its shaded envelope denote the mean and standard error of IRBC, while the blue solid line and its shaded envelope denote the mean and standard error of UVPM. Furthermore, owing to the relatively high wind speeds in the upper atmosphere, daytime measurements in this study generally did not reach the top of the PBL.

Vertical profiles of BC and UVPM concentrations reveal a consistent decrease with increasing altitude, with the most pronounced gradient observed in the near-surface layer. A comparative analysis of their vertical profiles reveals that during periods of weak convective activity, such as early morning and nighttime, UVPM concentrations aloft generally exceed those of BC, while near the surface the two species show much smaller differences. This elevated UVPM-to-BC ratio at altitude may be attributable to the lighter molecular weight and smaller size of gas-phase precursors compared to soot particles. Under nocturnal stable stratification, vertical mixing is suppressed, allowing volatile organic compounds (VOCs) to be lofted more readily into the free troposphere. There, in a relatively clean atmosphere lacking efficient coagulation sinks, NO_3^- dominated nighttime chemistry and low temperatures enhance secondary organic aerosol formation via low-temperature condensation and gas–particle partitioning (Han & Jang, 2023; Kuang et al., 2025; Kulmala, 2022; Morgan et al., 2009; Wang et al., 2023; Zhao et al., 2024). These processes collectively amplify the

https://doi.org/10.5194/egusphere-2025-3254
Preprint. Discussion started: 13 August 2025

UVPM–BC concentration difference at night. After sunrise, increased solar heating invigorates convection and erodes the nocturnal inversion at the boundary-layer top. Pollutants trapped in the residual layer are then entrained and mixed downward into the daytime boundary layer, reducing the UVPM–BC disparity while both profiles continue to decline with altitude (Zhao et al., 2023). Notably, between 14:00 and 17:00 LST, strong convective mixing homogenizes BC and UVPM within the 100–800 m layer; however, BC is not effectively transported to higher altitudes, resulting in a pronounced UVPM–BC difference aloft by 17:00. By approximately 20:00 LST, as convective activity wanes, the UVPM–BC concentration difference reemerges throughout the entire column and remains more pronounced at higher elevations than near the surface.

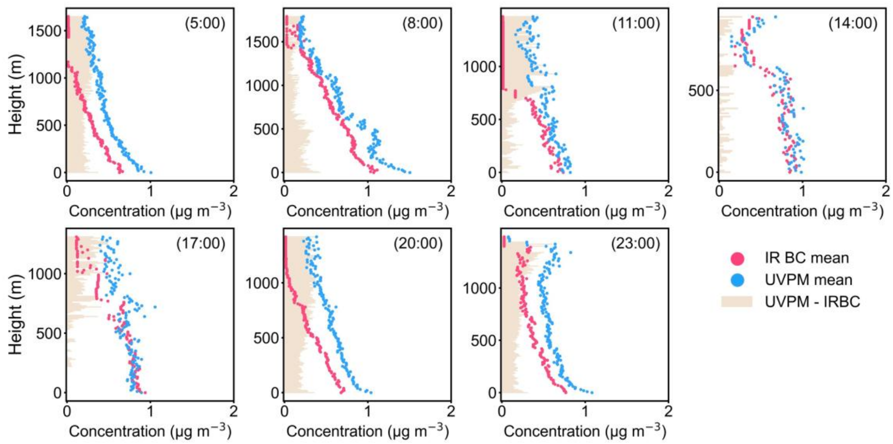

Figure 2. Diurnal variation of the average IRBC and UVPM concentration profiles in the Pingliang region. The red and blue curve represents IRBC and UVPM concentrations, respectively. The light beige shaded area represents the difference between UVPM and IRBC.

To better characterize BC vertical structure within the stable boundary layer, the observed profiles were classified into four types, each exhibiting distinct features. In Cluster 1, BC and UVPM decrease almost uniformly with altitude at a rate of approximately 0.51 μg m^{-3} km^{-1} up to 1000 m. Cluster 2 also shows comparable near-surface concentrations of both species, but with a rapid decline of about 1.23 μg m^{-3}

https://doi.org/10.5194/egusphere-2025-3254
Preprint. Discussion started: 13 August 2025

km⁻¹ below 250 m followed by a more gradual decrease above, reflecting a stronger nocturnal inversion that inhibits upward diffusion. Cluster 3 profiles, typically observed at 05:00, 08:00, and 20:00 LST under intense inversions, display a modest decrease of approximately 0.10 μg m^{-3} km^{-1} from the surface to 100 m, an unexpected increase in BC and UVPM between 100 and 600 m (attributable to pollutant accumulation and upward mixing within the deep neutral residual layer; Kulmala et al., 2023), and a decline above 600 m. In Cluster 4, concentrations remain nearly constant below 200 m but rise with height above this level, likely due to a weak neutral stratification between 200 and 400 m. Because these observations coincided with strong upper-level winds, measurements above approximately 400 m were curtailed to protect instrumentation, leaving open the question of whether Cluster 4 would exhibit a high-altitude decrease similar to Cluster 3.

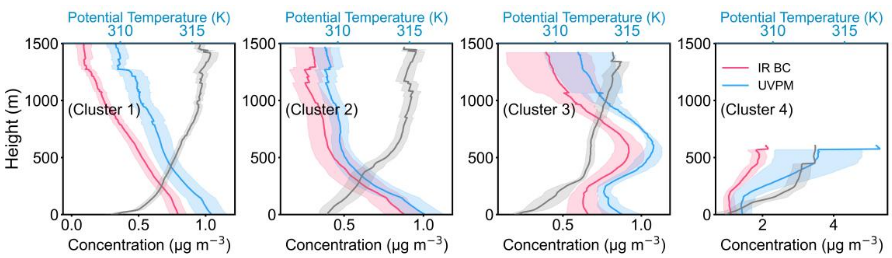

Figure 3. Cluster analysis of BC concentration profiles in the Pingliang region. The red curve represents IRBC, while the blue curve represents UVPM. The red and blue shaded areas indicate the standard errors of IRBC and UVPM, respectively.

3.1.3 Diurnal variations of AAE profiles

Figure S5 presents the variations of the light absorption coefficients of UVPM and BC at different altitudes. Overall, both UVPM and BC absorption coefficients decline steadily with increasing altitude, a pattern primarily controlled by the mass concentrations of carbonaceous aerosols. Moreover, the difference between the UVPM and BC absorption coefficients diminishes with height, indicating that UVPM dominates light absorption by carbonaceous aerosols in the lower atmosphere, whereas BC exerts a greater influence aloft, consistent with the findings of Qi et al.

(2025). The AAE, which characterizes the wavelength dependence of the mass-specific absorption by BC (calculation details are given in Figure S6), was calculated for the study period; the average diurnal AAE values are shown in Figure S7. Compared with Wu et al. (2021), the AAE of BC in Pingliang (1.65) is substantially higher than that reported for Shenzhen (<1.00). We further selected observations from representative pollution events to compare AAE under different weather conditions (Figure 4). During dust episodes, AAE increases markedly, by approximately 83% relative to dust-free conditions. Likewise, emissions from diesel vehicles yield higher AAE than periods without diesel contributions. Under heavy fog in the lowest 200 m, AAE is also elevated; at 200 m the rapid decrease in AAE likely results from the sharp reduction of water vapor aloft. Hence, compared with daytime, the lower frequency and intensity of anthropogenic activity at nighttime lead to a narrower range of aerosol sources and a smaller vertical variation in AAE across the entire profile.

Previous studies commonly employ a two-component model to differentiate the absorption Ångström exponent of black carbon (AAE_{BC}) and brown carbon (AAE_{BrC}), fixing AAE_{BC} at 1 and thereby deriving AAE_{BrC} (Figure S8). An AAE_{BrC} value greater than 2.0 is generally attributed to biomass burning and secondary aging processes. The diurnal AAE_{BrC} profiles shown in Figure S8 reveal pronounced contributions from secondary organic aerosol formation or from mixed emissions of biomass and fossil fuels at our observation site. Overall, daytime AAE_{BrC} values exceed those recorded at night and in the early morning, reflecting the stronger photochemical activity during daylight hours that promotes carbonaceous aerosol aging.

https://doi.org/10.5194/egusphere-2025-3254
Preprint. Discussion started: 13 August 2025

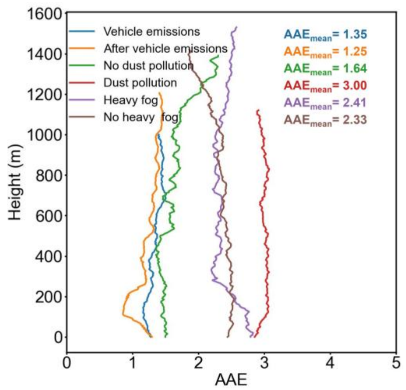

Figure 4. AAE profiles under different pollution conditions. (Vehicle emissions, After vehicle emissions, No dust pollution, Dust pollution, Heavy fog and No heavy fog occurred at 20:00 on July 17, 2024; 23:00 on July 17, 2024; 08:00 on July 20, 2024; 08:00 on July 21, 2024; 05:00 on July 25, 2024; and 05:00 on July 26, 2024, respectively.)

3.2 Thermodynamic impacts on profiles of BC and UVPM

Diurnal evolution of the PBLH is one of the primary factors controlling aerosol vertical distribution and is essential for understanding feedbacks between the boundary layer meteorology and aerosols. Zhang et al. (2020) reviewed and compared multiple PBLH retrieval methods. From the perspective of tracer distributions, PBLH inferred from vertical profiles of tracers such as water vapor and aerosols is termed the material PBLH ($PBLH_C$; Shi et al., 2020). Alternatively, PBLH can be derived from the vertical gradient of potential temperature ($PBLH_\theta$), with calculation protocols summarized in Table S1. Because PBLH evolves continuously, we selected a day with uninterrupted observations; however, owing to strong upper-level winds, continuous carbonaceous aerosol profiles were obtained only on 27 July 2024 at seven time slots (Figure 5). Hence, this day serves as a case study for examining how diurnal PBL evolution influences aerosol vertical structure. The parcel method is well suited to convective conditions but cannot accurately resolve $PBLH_\theta$ during early morning and nighttime (Holzworth, 1964), whereas it performs reliably under strong daytime convection. Using this approach, $PBLH_\theta$ at 11:00 and 17:00 LST were 508 m and 450 m, respectively; at 14:00, measurement ceilings did not reach $PBLH_\theta$. By

https://doi.org/10.5194/egusphere-2025-3254
Preprint. Discussion started: 13 August 2025

contrast, the potential-temperature gradient method yields accurate estimates at night and in the early morning: $PBLH_\theta$ at 05:00, 08:00, 20:00, and 23:00 LST were 260 m, 181 m, 260 m, and 223 m, respectively. A comparison of UVPM and BC profiles with these $PBLH_\theta$ values reveals that nighttime $PBLH_\theta$ from potential-temperature gradients exceeds the $PBLH_C$ inferred from aerosol distributions, a phenomenon also noted by Jiang et al. (2021). This discrepancy arises because nocturnal longwave radiative cooling and weakened turbulence enhance near-surface stability and often produce inversions; during their early development, $PBLH_\theta$ determined by potential-temperature gradients tends to overshoot the inversion top, whereas $PBLH_C$ more closely aligns with the inversion height.

Analysis of the potential-temperature profiles in Figure 5 indicates that at around 05:00 LST the planetary boundary layer top lay near 260 m. Below this altitude, both BC and UVPM concentrations decrease slightly with height. The potential-temperature profile further reveals a deep residual layer above the boundary-layer top, where colder near-surface air is trapped beneath warmer air aloft, creating a stable stratification that inhibits mixing within that layer and leads to increasing particle concentrations toward its base. In the transition to the free troposphere above the residual layer, comparatively low aerosol concentrations and enhanced turbulence promote further dilution, and beyond approximately 500 m BC and UVPM again decline with height. By 08:00 LST the boundary-layer height remained near 200 m, and the vertical variation in aerosol concentrations mirrored the pattern observed at 05:00. With increasing solar insolation, however, surface heating intensified convection so that by 11:00 LST the boundary-layer top had risen to roughly 500 m. During this stage, relatively small vertical gradients in BC and UVPM within the boundary layer indicate well-mixed conditions. At 14:00 LST tethered-balloon sampling did not reach the boundary-layer top, but observations within the layer show uniform aerosol distributions, preventing a direct assessment of boundary-layer-height effects on concentration profiles. The potential-temperature gradients between 11:00 and 14:00 LST exhibit significant fluctuations, signaling unstable stratification

https://doi.org/10.5194/egusphere-2025-3254
Preprint. Discussion started: 13 August 2025

favorable to vertical pollutant transport (Li, 2019). From 14:00 to 17:00 LST, as solar radiation waned and surface temperatures fell, the boundary-layer top subsided to about 450 m. At this time, potential temperatures within the boundary layer remained lower than at the surface and displayed pronounced variability, reflecting continued unstable stratification and strong vertical mixing; BC and UVPM maintained nearly uniform distributions. Above the boundary layer, a mixed layer approximately 300 m thick persisted; at its top, diminished turbulence inhibited aerosol dispersion, causing localized accumulation of BC and UVPM (Ding et al., 2016). By 20:00 LST, sunset-driven surface cooling weakened convection, a nocturnal inversion developed near the ground, and calm winds led to pollutant accumulation at low altitudes. As surface temperatures continued to drop, vertical transport further diminished, confining aerosols below roughly 200 m by 23:00 LST.

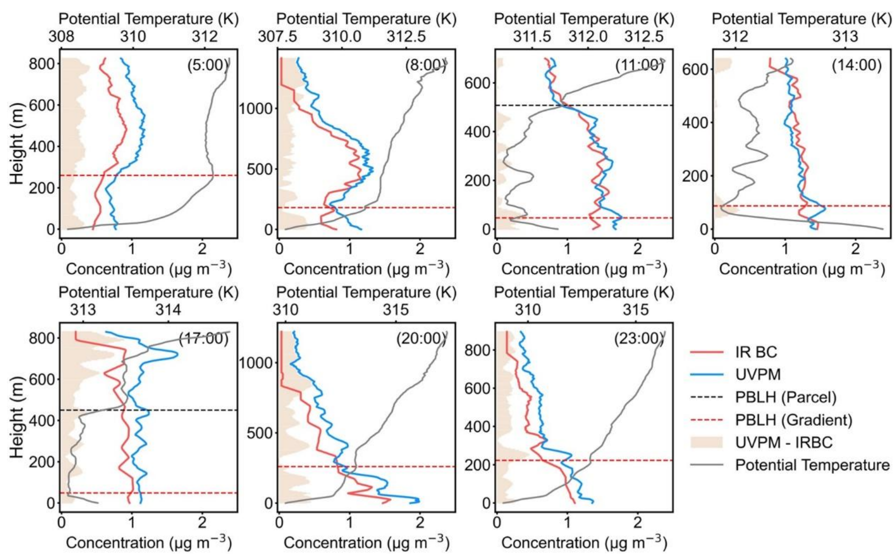

Figure 5. Diurnal variations of BC, UVPM and potential temperature profiles on July 27, 2024. The red curve represents IRBC, the blue curve represents UVPM, and the gray curve represents the potential temperature profile. The light beige shaded area represents the difference between IRBC and UVPM. The black and red dashed lines represent the PBLH calculated using the air parcel method and the potential temperature gradient method, respectively.

https://doi.org/10.5194/egusphere-2025-3254
Preprint. Discussion started: 13 August 2025

3.3 Dynamic impacts on profiles of BC and UVPM

3.3.1 Impacts of long-range transport on carbonaceous aerosols

Long-range transport of air masses plays a crucial role in shaping the vertical distribution of air pollutants. Figure S9 presents the 500 m trajectories and their altitude profiles for air masses arriving at the site during the observation period. It shows that, upon entering the Pingliang region, these air parcels generally descend to below 1500 m, meaning that, in addition to pollutants carried within the air mass itself, emissions from surrounding urban areas also significantly impact the receptor site. Trajectory-cluster analysis at 100 m, 500 m, and 1000 m (Figure 6) reveals that, in summer, Pingliang is principally influenced by air masses originating from Inner Mongolia and Ningxia to the north, from Gansu–Qingyang and northern Shaanxi to the east, and from southern Shaanxi to the south. At 500 m and 1000 m, regional contributions from these directions are broadly similar, whereas at 100 m the proportion of short-range flow from the southeast increases markedly. The shaded overlays in Figure 6 show the potential source contribution function (PSCF) and concentration-weighted trajectory (CWT) results for UVPM. PSCF indicates that air parcels from Inner Mongolia, Ningxia, Shanxi, and Shaanxi to the north, east, and south exert the greatest influence on the Pingliang site. Specifically, at 100 m the highest PSCF values occur along the Shaanxi–Gansu border, while at 500 m parcels from central Shaanxi and the Shanxi–Henan–Shaanxi nexus dominate, followed by the tri-provincial junction of Shaanxi, Gansu, and Sichuan. However, the CWT analysis identifies Hanzhong in southern Shaanxi as the most significant source region for UVPM at the receptor. Taken together, PSCF and CWT pinpoint southern Shaanxi cities and local emissions around Pingliang as major contributors to carbonaceous aerosol pollution, whereas at higher altitudes UVPM is primarily transported from the south. Overall, these source-apportionment results align with the conditional probability function (CPF) analysis, confirming that southerly flows contribute most substantially to UVPM concentrations at the observation site.

https://doi.org/10.5194/egusphere-2025-3254
Preprint. Discussion started: 13 August 2025

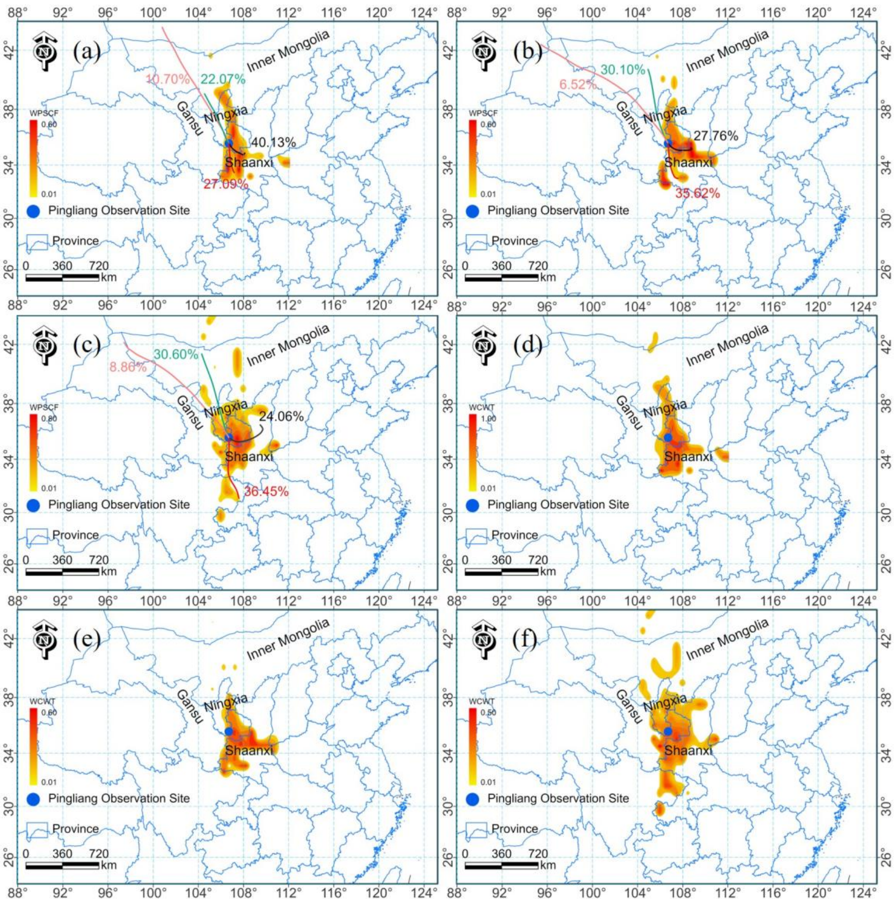

Figure 6. Backward trajectory clustering and PSCF analysis results of air masses at heights of a) 100, b) 500, and c) 1000 m during the observation period, respectively. CWT analysis results of air masses at heights of d) 100, e) 500, and f) 1000 m during the observation period, respectively.

3.3.2 Impacts of local sources on carbonaceous aerosols

In addition to long-range transport, local wind speed and direction significantly modulate the vertical distribution of aerosols at the observation site. Conditional Probability Function (CPF) plots, which relate pollutant concentrations to wind sectors and speeds, help elucidate these local transport and dispersion mechanisms. Figure 7 shows CPF diagrams for the 90th percentile of UVPM concentrations at 100 m, 500 m and 1000 m. The mean UVPM concentrations decrease with altitude, from

https://doi.org/10.5194/egusphere-2025-3254
Preprint. Discussion started: 13 August 2025

0.64 μg m^{-3} at 100 m, to 0.44 μg m^{-3} at 500 m, and to 0.31 μg m^{-3} at 1000 m, indicating that extreme UVPM events become less probable aloft. At 100 m, elevated UVPM levels are associated with southerly, southwesterly, northerly and northwesterly winds, reflecting both urban emissions and regional inflow. At 500 m, the influence of northwesterly, southwesterly and northerly sectors diminishes, while southerly winds remain the dominant driver of high UVPM, albeit with reduced effect. Southeasterly winds sporadically produce high UVPM at both 100 m and 500 m, likely linked to local point sources, but occur infrequently. Overall, southerly and southeasterly sectors exert the greatest influence on UVPM at all levels, consistent with the location of Pingliang's urban center directly south of the measurement site (Figure 1).

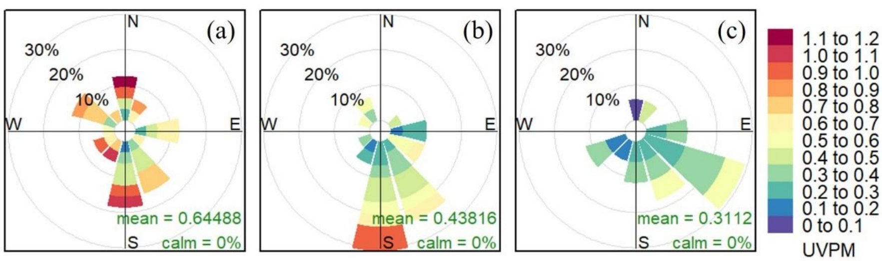

Figure 7. CPF (Conditional Probability Function) diagrams of the 90th percentile of the UVPM concentration with respect to wind speed and wind direction at the heights of a) 100, b) 500 and c) 1000 m.

To better compare the thermodynamically driven and dynamically driven influences on pollutant vertical distribution, this section again focuses on 27 July 2024 to examine the effects of wind speed and mechanical turbulence. Figure 8 presents horizontal and vertical wind speeds together with mechanical turbulence measured by the Doppler wind lidar during the sampling periods on that day. At 05:00 LST, both horizontal and vertical wind speeds within the boundary layer were low, while mechanical turbulence was comparatively high, promoting efficient vertical mixing and producing a nearly uniform distribution of carbonaceous aerosol concentrations throughout the boundary layer. In the residual layer above, stronger vertical winds

https://doi.org/10.5194/egusphere-2025-3254
Preprint. Discussion started: 13 August 2025

combined with weaker turbulence transported aerosols upward, causing UVPM and BC concentrations to increase with height between 400 and 600 m. At 08:00 LST, residual-layer concentrations exhibited a pattern similar to that at 05:00, but stronger vertical winds and reduced turbulence at the residual-layer top led to a more pronounced concentration decrease above the layer. By late morning, enhanced vertical wind speeds within the boundary layer facilitated upward transport of pollutants. However, at both 11:00 and 14:00 LST the aerosol concentration profile remained relatively uniform, with only a slight decrease with height; this reflects the competing effects of thermal convection, which lifts near-surface pollutants, and elevated turbulence aloft, which strengthens vertical exchange. At 17:00 LST, subsiding motions prevailed at 900–1200 m and mechanical turbulence index throughout the column was low, weakening vertical exchange and causing pollutants to accumulate near 800 m. By 20:00 LST, weak mechanical turbulence at the boundary-layer top and widespread subsidence near the surface suppressed upward transport of carbonaceous aerosols; as a result, pollutant concentrations decreased sharply with height within the boundary layer, while above the boundary-layer top horizontal and vertical winds aided dispersion, producing a continued decline in aerosol concentrations up to 800 m.

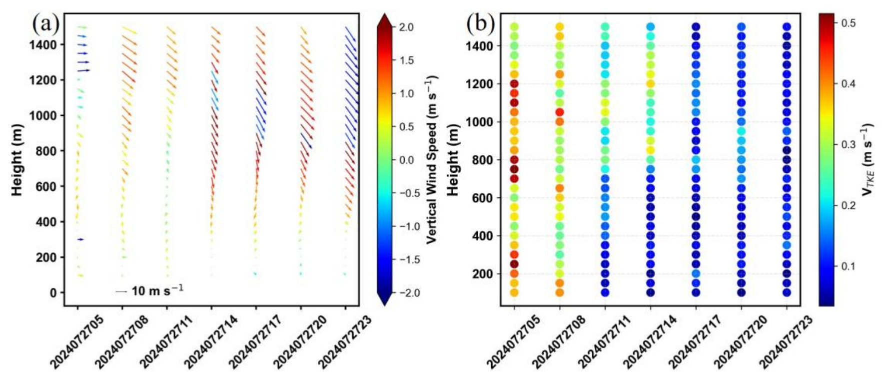

Figure 8. a) Vertical wind speed, horizontal wind speed and direction at 100–1500 m at the varying hours on July 27, 2024. The arrows indicate horizontal wind direction, with arrows pointing upward representing northerly winds. Arrow length represents horizontal wind speed magnitude. The color-shaded areas represent vertical wind speed. b) The V_{TKE} values at

https://doi.org/10.5194/egusphere-2025-3254
Preprint. Discussion started: 13 August 2025

varying altitudes, with distinct colors representing different V_{TKE} values.

To systematically investigate the mechanisms by which thermodynamic and dynamic processes influence the vertical distribution of carbonaceous aerosols, the observation periods were grouped into daytime (8:00, 11:00, 14:00 and 17:00 LST) and nighttime (20:00, 23:00 and 5:00 LST). A random forest nonlinear regression was applied to quantify the relative contributions of thermal forcing and dynamic forcing to the vertical concentration gradients of carbonaceous aerosols at different altitude layers (Figure 9). All regressions achieved coefficients of determination above 0.70, indicating good explanatory power. During daytime, these two processes exhibit clear vertical stratification. From the surface up to 600 m, thermal forcing dominates the evolution of aerosol concentration, whereas between 600 m and 1000 m horizontal wind speed is the primary driver. At night, the influence of thermal forcing is more complex. Between the surface and 300 m both thermal forcing and horizontal wind speed jointly govern vertical concentration variability. Between 300 m and 500 m, thermal forcing alone exerts decisive control, while above 500 m dynamic processes exert a much stronger influence than thermodynamic processes. Comparison with boundary layer height analyses shows that 300 m corresponds to the inversion top at night, where both thermodynamic and dynamic mechanisms contribute comparably to aerosol pollution. The layer from 300 m to 500 m largely coincides with the residual layer, which retains daytime turbulence characteristics and therefore responds more sensitively to thermal forcing. It should be noted that daytime measurements were taken at 08:00, 11:00 and 17:00 LST, a period when the boundary layer had not yet fully developed, so that 600 m approximately corresponds to the daytime boundary layer top. Consequently, within the daytime boundary layer, carbonaceous aerosol vertical distributions are mainly controlled by thermodynamic processes, in contrast to the thermodynamic dominance within the nocturnal residual layer. A schematic of these regulatory mechanisms for aerosol vertical structure is presented in Figure 10.

Li et al. (2019) also found through radiosonde observations that during the daytime,

https://doi.org/10.5194/egusphere-2025-3254
Preprint. Discussion started: 13 August 2025

thermodynamic processes induced unstable stratification within the boundary layer, resulting in well-mixed aerosols. In contrast, at night, the stable atmospheric stratification from the surface to 200 meters suppressed vertical dispersion of aerosols. Between 500 and 1000 meters, the presence of a low-level jet significantly influenced the vertical distribution of aerosols. In addition, strong mechanical turbulence played a key role in facilitating aerosol dispersion near the top of the boundary layer (Sun et al., 2024). These findings are consistent with the conclusions of this study.

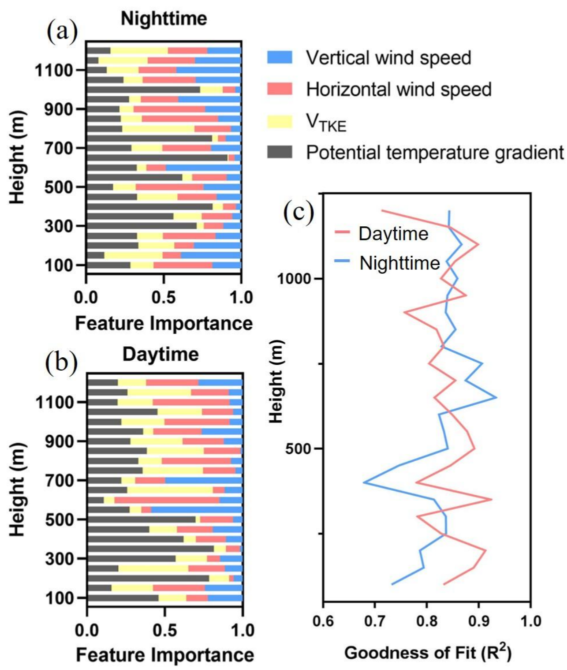

Figure 9. Results of feature importance analysis for the impacts of potential temperature gradient, mechanical turbulence, horizontal wind speed, and vertical wind speed on the UVPM gradient during a) nighttime and b) daytime, respectively. c) model goodness of fit (R^2) in the calculation.

https://doi.org/10.5194/egusphere-2025-3254
Preprint. Discussion started: 13 August 2025

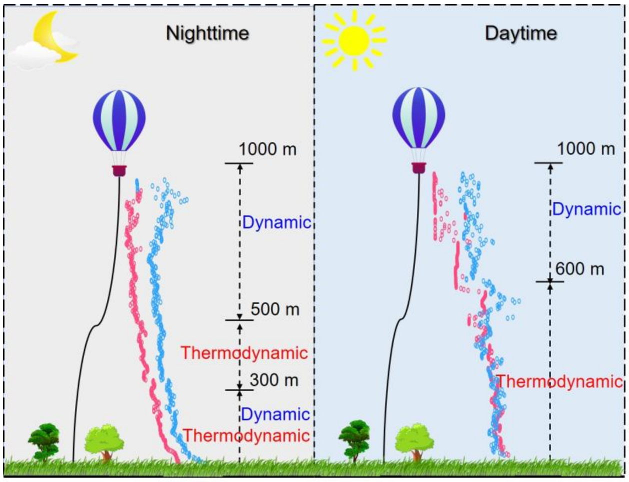

Figure 10. Schematic illustration of thermodynamic and dynamic impacts on aerosol vertical distribution. Within the figure, red circles denote IR BC concentrations, whereas blue circles denote UVPM concentrations; the more rightward a circle's position, the higher the corresponding concentration.

4. Conclusions

Pingliang City is situated on the Loess Plateau in northwestern China, where observational data on the vertical distribution of carbonaceous aerosols and meteorological parameters within the planetary boundary layer remain limited. To address this data gap, this study conducted detailed vertical profiling in a typical tableland region of the Loess Plateau using tethered balloons equipped with relevant observation instruments during July 2023 and July 2024.

The study found that near-surface concentrations of black carbon (BC) and ultraviolet-absorbing particulate matter (UVPM) in Pingliang were 0.10 μg m^{-3} and 0.12 μg m^{-3}, respectively. These concentrations are slightly lower than those reported for major Chinese cities including Beijing, Shanghai, Nanjing, Chengdu, Shenzhen, Hengshui, the Beibu Gulf region, and Lanzhou, as well as European cities such as Stuttgart in Germany and Milan in Italy. However, they are higher than the BC levels observed over the Tibetan Plateau and in the Arctic. A comparison of the vertical profiles of BC and UVPM showed that during early morning and nighttime periods, when convective activity is relatively weak, UVPM concentrations in the upper atmosphere are generally higher than those of BC. Near the surface, the difference between BC and UVPM concentrations is relatively small. This phenomenon is likely related to the formation of new particles in the upper atmosphere through gas to particle conversion of gaseous pollutants.

Analysis of thermodynamic and dynamic processes influencing the vertical distribution of carbonaceous aerosols shows that thermodynamic processes primarily govern vertical transport in the near-surface layer, while enhanced dynamic processes in the upper atmosphere promote horizontal dispersion of pollutants. The influence of thermodynamic and dynamic mechanisms on aerosol vertical profiles exhibits distinct stratification between daytime and nighttime. At various altitudes, air masses originating from the south are consistently associated with elevated UVPM concentrations. This pattern may be attributed to the combined influence of pollution sources located in the urban area to the south of the site and topographic differences along the north and south directions.

Nevertheless, there are still some limitations in this study that should be addressed in future work. Firstly, observations under strong wind conditions in the upper air were not successfully conducted during the campaign. Secondly, the study primarily focused on a limited set of air pollutants. Future research will incorporate additional gaseous pollutants such as SO_2, NO_2, O_3, and VOCs to enable a more comprehensive analysis of the chemical formation mechanisms and vertical distribution characteristics of aerosols. Furthermore, the filed campaign was conducted at only a site, and thus the feedbacks between aerosols and PBL meteorology cannot be fully understanded at whole Loess Plateau. The upcoming field campaign will be conducted at the other sites to better reveal the impact of thermodynamic and dynamic processes on the vertical profiles of air pollutants.

Author contributions. QS performed the data analysis and prepared the initial draft of the manuscript. SZ and YY designed the experimental approach and revised the manuscript. QS, SZ, LD, TZ, GZ, JL, XZ, and YL participated in data collection during the experiment.

Financial support. This work was supported by the National Natural Science Foundation of China (42422504), Major Science and Technology Project of Gansu Province (24ZD13FA003), and Excellent Member of Youth Innovation Promotion Association, Chinese Academy of Sciences (Y2021111), and Youth United Funding of Lanzhou Branch of Chinese Academy of Sciences.

References:

Allen, R. J., Landuyt, W. The vertical distribution of black carbon in CMIP5 models: Comparison to observations and the importance of convective transport. J. Geophys. Res.-Atmos., 119(8), 4808-4835, http://doi.org/10.1002/2014JD021595, 2014.

Bisht, D. S., Tiwari, S., Dumka, U. C., Srivastava, A. K., Safai, P. D., Ghude, S. D., Chate, D. M., Rao, P. S. P., Ali, K., Prabhakaran, T., Panickar, A. S., Soni, V. K., Attri, S. D., Tunved, P., Chakrabarty, R. K., Hopke, P. K. Tethered balloon-born and ground-based measurements of black carbon and particulate profiles within the lower troposphere during the foggy period in Delhi, India. Sci. Total Environ., 573, 894-905, http://doi.org/10.1016/j.scitotenv.2016.08.185, 2016.

Bond, T. C., Doherty, S. J., Fahey, D. W., Forster, P. M., Berntsen, T., DeAngelo, B. J., Flanner, M. G., Ghan, S., Kärcher, B., Koch, D., Kinne, S., Kondo, Y., Quinn, P. K., Sarofim, M. C., Schultz, M. G., Schulz, M., Venkataraman, C., Zhang, H., Zhang, S., Bellouin, N., Guttikunda, S. K., Hopke, P. K., Jacobson, M. Z., Kaiser, J. W., Klimont, Z., Lohmann, U., Schwarz, J. P., Shindell, D., Storelvmo, T., Warren, S. G., Zender, C. S. Bounding the role of black carbon in the climate system: A scientific assessment. J. Geophys. Res.-Atmos., 118(11), 5380-5552, http://doi.org/10.1002/jgrd.50171, 2013.

https://doi.org/10.5194/egusphere-2025-3254
Preprint. Discussion started: 13 August 2025

Chen, D. L., Liao, H., Yang, Y., Chen, L., Zhao, D. L., Ding, D. Simulated impacts of vertical distributions of black carbon aerosol on meteorology and $PM_{2.5}$ concentrations in Beijing during severe haze events. Atmos. Chem. Phys., 22(3), 1825-1844, http://doi.org/10.5194/acp-22-1825-2022, 2022.

Ding, A. J., Huang, X., Nie, W., Sun, J. N., Kerminen, V. M., Petäjä, T., Su, H., Cheng, Y. F., Yang, X. Q., Wang, M. H., Chi, X. G., Wang, J. P., Virkkula, A., Guo, W. D., Yuan, J., Wang, S. Y., Zhang, R. J., Wu, Y. F., Song, Y., Zhu, T., Zilitinkevich, S., Kulmala, M., Fu, C. B. Enhanced haze pollution by black carbon in megacities in China. Geophys. Res. Lett., 43(6), 2873-2879, http://doi.org/10.1002/2016GL067745, 2016.

Emeis, S., Schaefer, K., Muenkel, C. Surface-based remote sensing of the mixing-layer height - a review. Meteorol. Z., 17(5), 621-630, http://doi.org/10.1127/0941-2948/2008/0312, 2008.

Ferrero, L., Cappelletti, D., Busetto, M., Mazzola, M., Lupi, A., Lanconelli, C., Becagli, S., Traversi, R., Caiazzo, L., Giardi, F., Moroni, B., Crocchianti, S., Fierz, M., Močnik, G., Sangiorgi, G., Perrone, M. G., Maturilli, M., Vitale, V., Udisti, R., Bolzacchini, E. Vertical profiles of aerosol and black carbon in the Arctic: a seasonal phenomenology along 2 years (2011–2012) of field campaigns. Atmos. Chem. Phys., 16(19), 12601-12629, http://doi.org/10.5194/acp-16-12601-2016, 2016.

Ferrero, L., Mocnik, G., Ferrini, B. S., Perrone, M. G., Sangiorgi, G., Bolzacchini, E. Vertical profiles of aerosol absorption coefficient from micro-Aethalometer data and Mie calculation over Milan. Sci. Total Environ., 409(14), 2824-2837, http://doi.org/10.1016/j.scitotenv.2011.04.022, 2011.

Guan, X., Zhang, N. Y., Tian, P. F., Tang, C. G., Zhang, Z. D., Wang, L. G., Zhang, Y. S., Zhang, M., Guo, Y. M., Du, T., Cao, X. J., Liang, J. N., Zhang, L. Wintertime vertical distribution of black carbon and single scattering albedo in a semi-arid region derived from tethered balloon observations. Sci. Total Environ., 807, http://doi.org/10.1016/j.scitotenv.2021.150790, 2022.

Hagler, G. S. W., Yelverton, T. L. B., Vedantham, R., Hansen, A. D. A., Turner, J. R. Post-processing Method to Reduce Noise while Preserving High Time Resolution in Aethalometer Real-time Black Carbon Data. Aerosol Air Qual. Res., 11(5), 539-546,

https://doi.org/10.5194/egusphere-2025-3254
Preprint. Discussion started: 13 August 2025

http://doi.org/10.4209/aaqr.2011.05.0055, 2011.

Han, S., Jang, M. Modeling daytime and nighttime secondary organic aerosol formation via multiphase reactions of biogenic hydrocarbons. Atmos. Chem. Phys., 23(2), 1209-1226, http://doi.org/10.5194/acp-23-1209-2023, 2023.

Han, Y., Zhou, Y. W., Guo, J. P., Wu, Y. H., Wang, T. J., Zhuang, B. L., Li, M. M. The Characteristics of Spatial and Temporal Variations in the PBL during the Landfall of Tropical Cyclones across East China. J. Appl. Meteorol. Clim., 58(7), 1557-1572, http://doi.org/10.1175/JAMC-D-18-0131.1, 2019.

Hodnebrog, O., Myhre, G., Samset, B. H. How shorter black carbon lifetime alters its climate effect. Nat. Commun., 5(5), 7. http://doi.org/10.1038/ncomms6065, 2014.

Holzworth, G. C. Estimates of mean maximum mixing depths in the contiguous united states. Mon. Weather Rev., 92(5), 235-242, http://doi.org/10.1175/1520-0493(1964)092<0235:EOMMMD>2.3.CO;2, 1964.

Jiang, Y. Y., Xin, J. Y., Zhao, D. D., Jia, D. J., Tang, G. Q., Quan, J. N., Wang, M., Dai, L. D. Analysis of differences between thermodynamic and material boundary layer structure: Comparison of detection by ceilometer and microwave radiometer. Atmos. Res., 248, 105179, http://doi.org/10.1016/j.atmosres.2020.105179, 2021.

Kuang, Y., Luo, B., Huang, S., Liu, J. W., Hu, W. W., Peng, Y. W., Chen, D. H., Yue, D. L., Xu, W. Y., Yuan, B., Shao, M. Formation of highly absorptive secondary brown carbon through nighttime multiphase chemistry of biomass burning emissions. Atmos. Chem. Phys., 25(6), 3737-3752, http://doi.org/10.5194/acp-25-3737-2025, 2025.

Kulmala, M., Cai, R., Stolzenburg, D., Zhou, Y., Dada, L., Guo, Y., Yan, C., Petäjä, T., Jiang, J., Kerminen, V. M: The contribution of new particle formation and subsequent growth to haze formation, Environ. Sci.: Atmos., 2: 352–361, https://doi.org/10.1039/D1EA00096A, 2022.

Kulmala, M., Kokkonen, T., Ezhova, E., Baklanov, A., Mahura, A., Mammarella, I., Bäck, J., Lappalainen, H. K., Tyuryakov, S., Kerminen, V., Zilitinkevich, S., Petäjä, T. Aerosols, Clusters, Greenhouse Gases, Trace Gases and Boundary-Layer Dynamics: on Feedbacks and Interactions. Boundary Layer Meteorol., 186(3), 475-503, http://doi.org/10.1007/s10546-022-00769-8, 2023.

https://doi.org/10.5194/egusphere-2025-3254
Preprint. Discussion started: 13 August 2025

Li, X. L., Ma, Y. J., Wang, Y. F., Wei, W., Zhang, Y. H., Liu, N. W., Hong, Y. Vertical Distribution of Particulate Matter and its Relationship with Planetary Boundary Layer Structure in Shenyang, Northeast China. Aerosol Air Qual. Res., 19(11), 2464-2476, https://doi.org/10.4209/aaqr.2019.06.0311, 2019.

Li, Y. Study on Vertical Atmospheric Observation Based on Tethered Balloon Platform in Wuqing Aera[D], Chinese Research Academy of Environmental Sciences, Beijing. https://link.cnki.net/doi/10.27510/d.cnki.gzhky.2019.000016, 2019.

Liu, B., Wu, C., Ma, N., Chen, Q., Li, Y. W., Ye, J. H., Martin, S. T., Li, Y. J. Vertical profiling of fine particulate matter and black carbon by using unmanned aerial vehicle in Macau, China. Sci. Total Environ., 709, 136109, http://doi.org/10.1016/j.scitotenv.2019.136109, 2020.

Lu, Y., Zhu, B., Huang, Y., Shi, S. S., Wang, H. L., An, J. L., Yu, X. N. Vertical distributions of black carbon aerosols over rural areas of the Yangtze River Delta in winter. Sci. Total Environ., 661, 1-9, http://doi.org/10.1016/j.scitotenv.2019.01.170, 2019.

Mazzola, M., Busetto, M., Ferrero, L., Viola, A. P., Cappelletti, D. AGAP: an atmospheric gondola for aerosol profiling. Rendiconti Lincei-Scienze Fisiche E Naturali, 27(Suppl 1), 105-113, http://doi.org/10.1007/s12210-016-0514-x, 2016.

Moorthy, K. K., Babu, S. S., Sunilkumar, S. V., Gupta, P. K., Gera, B. S. Altitude profiles of aerosol BC, derived from aircraft measurements over an inland urban location in India. Geophys. Res. Lett., 31(22), http://doi.org/10.1029/2004GL021336, 2004.

Morgan, W. T., Allan, J. D., Bower, K. N., Capes, G., Crosier, J., Williams, P. I., Coe, H. Vertical distribution of sub-micron aerosol chemical composition from North-Western Europe and the North-East Atlantic. Atmos. Chem. Phys., 9, 5389–5401, https://doi.org/10.5194/acp-9-5389-2009, 2009.

Panicker, A. S., Pandithurai, G., Safai, P. D., Dipu, S., Prabha, T. V., Konwar, M. Observations of black carbon induced semi direct effect over Northeast India. Atmos. Environ., 98, 685-692, http://doi.org/10.1016/j.atmosenv.2014.09.034, 2014.

Petaja, T., Jarvi, L., Kerminen, V. M., Ding, A. J., Sun, J. N., Nie, W., Kujansuu, J., Virkkula, A., Yang, X. Q., Fu, C. B., Zilitinkevich, S., Kulmala, M. Enhanced air pollution via aerosol-boundary layer feedback in China. Sci. Rep., 6, 18998,

https://doi.org/10.5194/egusphere-2025-3254
Preprint. Discussion started: 13 August 2025

http://doi.org/10.1038/srep18998, 2016.

Qi, S. F., Zhao, S. P., Yu, Y., Kang, S. C. Optical properties of carbonaceous aerosols and source impacts in the Lanzhou valley: In-situ observations by means of topographical relief. Urban Clim., 59, 102302, http://doi.org/10.1016/j.uclim.2025.102302, 2025.

Ramanathan, V., Carmichael, G. Global and regional climate changes due to black carbon. Nat. Geosci., 1(4), 221-227, http://doi.org/10.1038/ngeo156, 2008.

Ran, L., Deng, Z. Z., Xu, X. B., Yan, P., Lin, W. L., Wang, Y., Tian, P., Wang, P. C., Pan, W. L., Lu, D. R. Vertical profiles of black carbon measured by a micro-aethalometer in summer in the North China Plain. Atmos. Chem. and Phys., 16(16), 10441-10454, http://doi.org/10.5194/acp-16-10441-2016, 2016.

Samad, A., Vogt, U., Panta, A., Uprety, D. Vertical distribution of particulate matter, black carbon and ultra-fine particles in Stuttgart, Germany. Atmos. Pollut. Res., 11(8), 1441-1450, http://doi.org/10.1016/j.apr.2020.05.017, 2020.

Samset, B. H., Myhre, G. Vertical dependence of black carbon, sulphate and biomass burning aerosol radiative forcing. Geophys. Res. Lett., 38, 5, http://doi.org/10.1029/2011GL049697, 2011.

Schwarz, J. P., Weinzierl, B., Samset, B. H., Dollner, M., Heimerl, K., Markovic, M. Z., Perring, A. E., Ziemba, L. Aircraft measurements of black carbon vertical profiles show upper tropospheric variability and stability. Geophys. Res. Lett., 44(2), 1132-1140, http://doi.org/10.1002/2016GL071241, 2017.

Seibert, P., Beyrich, F., Gryning, S. E., Joffre, S., Rasmussen, A., Tercier, P. Review and intercomparison of operational methods for the determination of the mixing height. Atmos. Environ., 34(7), 1001-1027, http://doi.org/10.1016/S1352-2310(99)00349-0, 2000.

Seidel, D. J., Ao, C. O., Li, K. Estimating climatological planetary boundary layer heights from radiosonde observations: Comparison of methods and uncertainty analysis. J. Geophys. Res.-Atmos., 115(D16), D16113, http://doi.org/10.1029/2009JD013680, 2010.

Shi, S. S., Zhu, B., Lu, W., Yan, S. Q., Fang, C. W., Liu, X. H., Liu, D. Y., Liu, C. Estimation of radiative forcing and heating rate based on vertical observation of black carbon in Nanjing, China. Sci. Total Environ., 756, 11,

https://doi.org/10.5194/egusphere-2025-3254
Preprint. Discussion started: 13 August 2025

http://doi.org/10.1016/j.scitotenv.2020.144135, 2021.

Shi, Y., Hu, F., Xiao, Z. S., Fan, G. Q., Zhang, Z. Comparison of four different types of planetary boundary layer heights during a haze episode in Beijing. Sci. Total Environ., 711, 134928, http://doi.org/10.1016/j.scitotenv.2019.134928, 2020.

Sun, X. Y., Zhou, Y., Zhao, T. L., Fu, W. K., Wang, Z., Shi, C. N., Zhang, H., Zhang, Y. Q., Yang, Q. J., Shu, Z. Z. Vertical distribution of aerosols and association with atmospheric boundary layer structures during regional aerosol transport over central China. Environ. Pollut., 362, 124967, https://doi.org/10.1016/j.envpol.2024.124967, 2024.

Wang, D. F., Huo, J. T., Duan, Y. S., Zhang, K., Ding, A. J., Fu, Q. Y., Luo, J. H., Fei, D. N., Xiu, G. L., Huang, K. Vertical distribution and transport of air pollutants during a regional haze event in eastern China: A tethered mega-balloon observation study. Atmos. Environ., 246, 118039, http://doi.org/10.1016/j.atmosenv.2020.118039, 2021a.

Wang, H. C., Wang, H. L., Lu, X., Lu, K. D., Zhang, L., Tham, Y. J., Shi, Z. B., Aikin, K., Fan, S. J., Brown, S. S., Zhang, Y. H. Increased night-time oxidation over China despite widespread decrease across the globe. Nat. Geosci., 16: 217-223, https://doi.org/10.1038/s41561-022-01122-x, 2023.

Wang, H. L., Liu, A. K., Zhen, Z. X., Yin, Y., Li, B., Li, Y. Y., Chen, K., Xu, J. P. Vertical Structures of Meteorological Elements and Black Carbon at Mt. Tianshan Using an Unmanned Aerial Vehicle System. Remote Sens., 13(7), 1267, http://doi.org/10.3390/rs13071267, 2021b.

Wang, M., Xu, B. Q., Yang, S., Gao, J., Zhang, T. H., He, Z. Q., Kobal, M., Hansen, A. D. A. Black carbon profiles from tethered balloon flights over the southeastern Tibetan Plateau. Chin. Sci. Bull., 64(27): 2949-2958, https://doi.org/10.1360/TB-2019-0101, 2019.

Wang, Y. Q. MeteoInfo: GIS software for meteorological data visualization and analysis. Meteorol. Appl., 21(2), 360-368. http://doi.org/10.1002/met.1345, 2014.

Wang, Z. L., Huang, X., Ding, A. J. Dome effect of black carbon and its key influencing factors: a one-dimensional modelling study. Atmos. Chem. Phys., 18(4), 2821-2834, http://doi.org/10.5194/acp-18-2821-2018, 2018a.

Wang, Q. Q., Sun, Y. L., Xu, W. Q., Du, W., Zhou, L. B., Tang, G. Q., Chen, C., Cheng, X. L., Zhao, X. J., Ji, D. S., Han, T. T., Wang, Z., Li, J., Wang, Z. F. Vertically resolved

https://doi.org/10.5194/egusphere-2025-3254
Preprint. Discussion started: 13 August 2025

characteristics of air pollution during two severe winter haze episodes in urban Beijing, China. Atmos. Chem. Phys., 18(4), 2495-2509, http://doi.org/10.5194/acp-18-2495-2018, 2018b.

Wendisch, M., Hellmuth, O., Ansmann, A., Heintzenberg, J., Engelmann, R., Althausen, D., Eichler, H., Müller, D., Hu, M., Zhang, Y. Radiative and dynamic effects of absorbing aerosol particles over the Pearl River Delta, China. Atmos. Environ., 42(25), 6405-6416, http://doi.org/10.1016/j.atmosenv.2008.02.033, 2008.

Wu, C., Liu, B., Wu, D., Yang, H. L., Mao, X., Tan, J., Liang, Y., Sun, J. Y., Xia, R., Sun, J. R., He, G. W., Li, M., Deng, T., Zhou, Z., Li, Y. J. Vertical profiling of black carbon and ozone using a multicopter unmanned aerial vehicle (UAV) in urban Shenzhen of South China. Sci. Total Environ., 801, http://doi.org/10.1016/j.scitotenv.2021.149689, 2021.

Xie, C. H., Xu, W. Q., Wang, J. F., Wang, Q. Q., Liu, D. T., Tang, G. Q., Chen, P., Du, W., Zhao, J., Zhang, Y. J., Zhou, W., Han, T. T., Bian, Q. Y., Li, J., Fu, P. Q., Wang, Z. F., Ge, X. L., Allan, J., Coe, H., Sun, Y. L. Vertical characterization of aerosol optical properties and brown carbon in winter in urban Beijing, China. Atmos. Chem. Phys., 19(1), 165-179, http://doi.org/10.5194/acp-19-165-2019, 2019.

Yang, X. Y., Ji, D. S., Li, J. W., He, J., Gong, C. S., Xu, X. J., Wang, Z., Liu, Y., Bi, F., Zhang, Z. Z., Chen, Y. B. Impacts of springtime biomass burning in Southeast Asia on atmospheric carbonaceous components over the Beibu Gulf in China: Insights from aircraft observations. Sci. Total Environ., 857, 10, http://doi.org/10.1016/j.scitotenv.2022.159232, 2023.

Yang, Y., Zhao, D. L., Huang, Y., Tian, P., Liu, D. T., Huang, M. Y., He, H., Ding, D. P., Li, Y. Y., Zhao, C. Effects of black carbon aerosol on air quality and vertical meteorological factors in early summer in Beijing. Sci. Total Environ., 847, 10, http://doi.org/10.1016/j.scitotenv.2022.157529, 2022.

Zarzycki, C. M., Bond, T. C. How much can the vertical distribution of black carbon affect its global direct radiative forcing? Geophys. Res. Lett., 37(20), http://doi.org/10.1029/2010GL044555, 2010.

Zawadzka, O., Posyniak, M., Nelken, K., Markuszewski, P., Chilinski, M. T., Czyzewska, D., Lisok, J., Markowicz, K. M. Study of the vertical variability of aerosol properties based on cable cars in-situ measurements. Atmos. Pollut. Res., 8(5), 968-978, http://doi.org/10.1016/j.apr.2017.03.009, 2017.

Zhang, H. S., Zhang, X. Y., Li, Q. H., Cai, X. H., Fan, S. J., Song, Y., Hu, F., Che, H. Z., Quan, J. N., Kang, L., Zhu, T. Research progress on estimation of atmospheric boundary layer height. Acta Meteorol. Sin., 78(3), 522-536, http://doi.org/10.11676/qxxb2020.044, 2020.

Zhang, Y. Z., Forrister, H., Liu, J. M., Dibb, J., Anderson, B., Schwarz, J. P., Perring, A. E., Jimenez, J. L., Campuzano-Jost, P., Wang, Y. H., Nenes, A., Weber, R. J. Top-of-atmosphere radiative forcing affected by brown carbon in the upper troposphere. Nat. Geosci., 10(7), 486, http://doi.org/10.1038/NGEO2960, 2017.

Zhao, D. D., Xin, J. Y., Gong, C. S., Quan, J. N., Wang, Y. S., Tang, G. Q., Ma, Y. X., Dai, L. D., Wu, X. Y., Liu, G. J., Ma, Y. J. The impact threshold of the aerosol radiative forcing on the boundary layer structure in the pollution region. Atmos. Chem. Phys., 21(7), 5739-5753, http://doi.org/10.5194/acp-21-5739-2021, 2021.

Zhao, S. P., He, J. J., Dong, L. X., Qi, S. F., Yin, D. Y., Chen, J. B., Yu, Y. Contrasting Vertical Circulation between Severe and Light Air Pollution inside a Deep Basin Results from the Collaborative Experiment of 3D Boundary-Layer Meteorology and Pollution at the Sichuan Basin (BLMP-SCB). Bull. Am. Meteorol. Soc., 104(2), E411-E434, http://doi.org/10.1175/BAMS-D-22-0150.1, 2023.

Zhao, S. P., Qi, S. F., Yu, Y., Kang, S. C., Dong, L. X, Chen, J. B., Yin, D. Y. Measurement report: Contrasting elevation-dependent light absorption by black and brown carbon: lessons from in situ measurements from the highly polluted Sichuan Basin to the pristine Tibetan Plateau. Atmos. Chem. Phys., 22(22), 14693-14708, http://doi.org/10.5194/acp-22-14693-2022, 2022.

Zhao, S. P., Yu, Y., Yin, D. Y., Yu, Z. S., Dong, L. X., Mao, Z. L., He, J. J., Yang, J. C., Li, P., Qin, D. H. Concentrations, optical and radiative properties of carbonaceous aerosols over urban Lanzhou, a typical valley city: Results from in-situ observations and numerical model. Atmos. Environ., 213, 470-484, http://doi.org/10.1016/j.atmosenv.2019.06.046, 2019.

Zhao, S. P., Yu, Y., He, J. J., Dong, L. X., Qi, S. F. A New Physical Mechanism of Rainfall

https://doi.org/10.5194/egusphere-2025-3254
Preprint. Discussion started: 13 August 2025

Facilitation to New Particle Formation. Geophys. Res. Lett., 51(1), e2023GL106842, https://doi.org/10.1029/2023GL106842, 2023.